DOI: 10.1002/fuce.201600153

Microwave-assisted Synthesis of Pd Oxide-rich Pd Particles on Nitrogen/Sulfur Co-Doped Graphene with Remarkably Enhanced Ethanol Electrooxidation

J. X. Zhang[1], X. L. Yang[1]*, H. F. Shao[2], C. C. Tseng[1], D. S. Wang[1], S. S. Tian[1], W. J. Hu[1], C. Jing[1], J. N. Tian[1], Y. C. Zhao[1]*

[1] College of Chemistry and Pharmacy, Guangxi Normal University, Guilin 541004, PR China
[2] Shandong Non-Metallic Materials Institute, Jinan 250031, PR China

Received September 01, 2016; accepted November 18, 2016; published online December 19, 2016

Abstract

Nitrogen and sulfur co-doped graphene supported Pd oxide-rich (PdO_x-rich) Pd nanoparticles (Pd/NS-rGO) are synthesized by microwave-assisted ascorbic acid reduction method. Raman spectrum reveals that the introduced NS co-doping could introduce more defects on the graphene surface. X-ray diffraction, X-ray photoelectron spectrum, SEM and TEM images indicate that the synthesized PdO_x-rich Pd particles are well-dispersed on NS co-doped graphene surface. Cyclic voltammograms curves illustrate that the Pd/NS-rGO catalyst exhibits a larger electrochemically active surface area ($35.7\,m^2\,g^{-1}$) and higher positive current density (1,054.0 mA mg^{-1} Pd) than other catalysts prepared by similar methods. The Pd/NS-rGO catalyst also reveals superior anti-poisoning intermediate species ability and amazing stability. The electrocatalytic mechanism is also detailedly discussed and the designed Pd/NS-rGO catalyst has opened up a new insight and methodology for the construction of a high performance and stability ethanol electrocatalysts in corrosive alkaline environments.

Keywords: Direct Ethanol Fuel Cells, Electrocatalysis, Microwave-assisted, NS Co-doped Graphene, Pd Particles

1 Introduction

With the rapid increase in energy demand and growing concerns about environmental pollution, research on renewable and green energy sources has attracted considerable interest in the past decades [1–4]. Amongst various candidates, direct ethanol fuel cells (DEFCs) possess notable features including simple design, easy storage, good stability, high energy conversion efficiency, environmental-friendly character and low proton exchange membrane permeability, etc. [5–7]. Those characteristics continually soar the global attention to DEFCs to new highs. In addition, the kinetics of ethanol oxidation in alkaline medium is faster and DEFCs tend to be less corrosive than those in acidic medium [8–11]. Despite the significant advantages, there are still some major drawbacks for DEFCs. The complete oxidation of ethanol is extremely difficult and involves in some complex mechanism, such as cleavage of C-C bond, transference of 12 electrons and elimination of CO, CH_X-intermediates, which will poison the catalyst [12, 13]. Therefore, it is of great importance to design economic electrocatalysts with improved electrocatalytic performance, kinetic efficiency and stability [14, 15]. However, the low abundance and easy poisoning properties of platinum-related catalysts have seriously hindered their commercial applications in fuel cells [16, 17]. Alternatively, theoretical and experimental investigations demonstrated that Pd-based catalysts could overcome these obstacles and have aroused tremendous attention [18, 19]. Although Pd particles show good catalytic behav-

[*] *Corresponding author, xiulin.yang@kaust.edu.sa, yanchunzhao@aliyun.com*

iors for many useful reactions under different reaction conditions, the particles are prone to aggregation and form Pd black because of their high surface energy [20, 21]. Therefore, the immobilization of Pd particles on various supports is regarded as one of the most practical ways to address this problem.

Over the past decade, graphene has triggered tremendous interest due to its high electron mobility, excellent mechanical flexibility, specific surface area and unique optical properties [22, 23]. But most of the pristine graphene are subjected to chemical inertness and it remains urgent to modify the chemical properties of graphene by functionalization or surface modification to expand its application [24, 25]. Recently, heteroatom doping of graphene displays exceptional properties and characteristics. In the process of substitutional doping, carbon atoms in the skeleton are replaced by heteroatoms and the graphene structure are destroyed [26, 27]. Up to now, many techniques have been developed to obtain heteroatom-doped graphene, in which solvothermal and hydrothermal treatments are deemed to be a most facile and economic way to synthesize heteroatoms doped graphene [28]. It is interesting to note that introduction of nitrogen and sulfur, both with rich electrons, can change the π-conjugated system of graphene and alter the carbon structures. This will it will generate more defects and nuclear sites which can act as anchoring sites for metal particles [29], and then strengthen the interaction between metal particles and graphene supports and benefit the transformation of electron from supports to metal catalysts [30]. Currently, most of the published NS-doped carbon materials show superb performance in oxygen reduction reactions, formic acid oxidation, Li-ion batteries, etc. [31–33]. Until now, only few papers related to noble metals on NS co-doped graphene for alkaline ethanol electro-oxidation are published.

In this paper, we present a facile route to prepare NS dual-doped graphene by using ammonium chloride and sodium thiocyanate as precursors, and subsequently conduct microwave-assisted ascorbic acid reduction to prepare a highly dispersed PdO_x-rich Pd/NS-rGO catalyst. The introduction of N and S in graphene structure could generate abundant active sites for well-dispersing PdO_x-rich Pd particles on NS functionalized graphene surface. The synthesized Pd/NS-rGO catalyst exhibits larger electrochemically active surface area (EAS, 35.7 $m^2\ g^{-1}$) and higher positive current density (1,054.0 mA mg^{-1} Pd) than other similar method prepared catalysts. In addition, the Pd/NS-rGO catalyst also reveals superior anti-poisoning intermediate species ability and amazing stability.

2 Experimental

2.1 Preparation of GO and Reduced-GO

A modified Hummers method was used to prepare Graphene oxide (GO). Briefly, graphite powder (1.0 g) and NaCl (20.0 g) were thoroughly mixed by milling in mortar for 30 min. After rinsed with deionized water, the mixture was dried overnight at 60 °C, then added H_2SO_4 (98%) to the dried material and stirred the mixture for 24 h at room temperature. Subsequently, $KMnO_4$ (0.5 g) was slowly added into the mixture with stirring at 40 °C for 30 min. Then, the mixture was diluted with 140 mL deionized water at ambient temperature. One hour later, another H_2O (140 mL) and H_2O_2 (10 mL) was added into the mixture. Upon treatment with peroxide, the suspension was centrifuged, washed and dried overnight to obtain GO. The prepared GO was then put into a furnace and kept at 700 °C in N_2 for 1 h. The reduced-GO (rGO) was obtained and left for further treatment.

2.2 Synthesis of NS-rGO

rGO (30 mg), NaSCN (160 mg), NH_4Cl (106 mg) were dispersed in distilled water under ultrasonic treatment. Then, the suspension was transferred into Teflon-lined stainless steel autoclave and hydrothermal treatment at 180 °C for 12 h. Afterwards, the mixture was centrifuged, rinsed, dried to obtain NS-rGO. Similar steps were also applied to prepare N-rGO, except for adding NaSCN in the whole process.

2.3 Preparation of Pd/NS-rGO

For the synthesis of Pd/NS-rGO, a certain amount of H_2PdCl_4 (Pd: 5 mg), NS-rGO (20 mg), sodium citrate (20 mg) and ascorbic acid (20 mg) were simultaneously dissolved in 50 mL water under ultrasonic treatment and further treated with microwave heating in 800 W for 30 s to achieve Pd/NS-rGO. For comparison, Pd/N-rGO, Pd/CNTs and Pd/XC-72 were prepared by the same procedure.

2.4 Characterization

The morphology and micro-structure of the synthesized samples were observed with scanning electron microscope (SEM) and transmission electron microscopy (TEM) (Hitachi H-800, Japan). X-ray diffraction (XRD) analyses were carried out with a RigakuD/MAX 2500v/pc (Japan) diffractometer using Cu Kα source. Raman spectroscopy (inVia, Renishaw, England) was used to investigate the integrity and electronic structure of the carbon materials. The chemical valences of metals in the catalysts were analyzed by X-ray photoelectron spectroscopy (XPS) (JPS-9010TR, Japan) with Mg Ka radiation.

2.5 Electrochemical Measurements

All electrochemical experiments were performed with a conventional three-electrode system using a CHI660D electrochemical working station (CH Instrument, Inc.) at room temperature. Firstly, the glassy carbon electrode (GCE) was polished by using a-Al2O3, and then excessively washed using deionized water and ethanol. The as-prepared catalysts were ultrasonically dispersed into H_2O/C_2H_5OH solution, and then deposited onto the polished GCE. After natural drying at room temperature, 10 μL 0.5% Nafion in ethanol solution was

dropped to fix the catalysts on GCE. All the potentials are referred to the saturated calomel electrode (SCE) in this work. A Pt foil and SCE were employed as a counter electrode and a reference electrode, respectively. The cyclic voltammogram (CV) measurement was firstly carried out in a solution of 0.5M NaOH at a scan rate of 50 mV s^{-1} from –0.8 V to 0.4 V, in order to calculate the electrochemical active surface areas (EAS) of the catalysts. Afterwards, electrooxidation of ethanol was investigated by CV measurements with the same scan rate between –0.8 V to 0.4 V in a solution of 0.5M NaOH + 1.0M C_2H_5OH. Chrono-amperometry measurements were then performed at a fixed potential of 0.2 V for 7,200 s in 0.5M NaOH + 1.0M C_2H_5OH solution. The metal loading was kept at 70.8 μg cm^{-2} and all tests were conducted at ambient temperature (25 ± 0.5 °C).

3 Results and Discussion

The NS dual-doped graphene was synthesized *via* hydrothermal treatment of the obtained rGO from GO together with NaSCN and NH_4Cl in water solution, as illustrated in Scheme 1. The hydrothermal treatment could induce the thermal decomposition of NaSCN and NH_4Cl at high temperature and pressure conditions. The generated fragments of N and S will strongly attack the structure of graphene, and the formed different groups will be effectively functionalized or non-functionalized on the graphene structures. The NS dual-doped graphene was then ultrasonically mixed with H_2PdCl_4, sodium citrate and ascorbic acid at room temperature. The sodium citrate is used as stabilizing agent and the ascorbic acid is regarded as reducing agent. The mixed solution was then put into microwave reactor in a beaker at a power of 800 W for 30 s. The microwave reactor could rapidly increase the temperature of the mixture solution, promote dispersion of solutes and accelerate the completion of the whole reaction.

Raman spectroscopy was used to gauge the extent of disorder and degree of the prepared NS-rGO and rGO. As shown in Figure 1A, there are two distinct peaks including G-band with E_{2g} symmetry roughly located at 1,581 cm^{-1} ascribed to ordered sp^2 hybridized graphitic carbon atoms and D-band with A_{1g} symmetry at about 1,354 cm^{-1} arising from disordered sp^3 defect sites, amorphous carbon or edges defects, etc. [34]. The intensity of I_D/I_G reflects the structure defects and edge plane exposure, and it is usually adopted to evaluate the doping and defects in carbon materials. A higher ratio of I_D/I_G indicates higher defects, and lower value signifies lower disorder in the graphitic lattice. It can be clearly seen that the I_D/I_G ratio of NS-rGO (0.99) is larger than that of rGO (0.57). On the other hand, it is well known that the D′-band is also associated with defects and disorder in carbon structure [35]. Thus, the largest I_D/I_G ratio and the enhancement of the D′-band of the NS-rGO imply that NS-rGO contains more amorphous carbon impurities than rGO [36]. In this case, those defects will in turn act as active sites and reinforce the interaction between Pd particles and support, and thus increase the catalysts loading and particles dispersion.

X-ray diffraction (XRD) was used to monitor the crystal structures of Pd/NS-rGO together with Pd/N-rGO, Pd/CNTs and Pd/XC-72. As shown in Figure 1B, all samples displayed five similar diffraction peaks at 2θ of approximately 40.1°, 46.7°, 68.1°, 82.1° and 86.6°, which can be well indexed to face-centered cubic (fcc) crystalline Pd (JCPDS: 65-2867) [37, 38]. It should be noted that, compared to Pd/N-rGO, Pd/CNTs and Pd/XC-72, Pd/NS-rGO shows several additional peaks which can be ascribed to the tetragonal structure of PdO (JCPDS: 43-1024). It means that the support of NS-rGO is much more beneficial to form PdO composition than others. This can be explained that the groups of N, S on rGO have a stronger binding force with Pd precursor, and thus it could suppress the reduction of the precursor to some extent. After microwave heating treatment, the resulted high temperature is more tending to form PdO composition. In addition, a narrow peak around 26° for Pd/NS-rGO can be assigned to the (002) characteristic diffraction peak of hexagonal crystalline graphite [39], which is consistent with Pd/CNTs composite. However, there is a broad peak at *ca.* 24.9° on Pd/N-rGO, which is a typical characteristics of stacked graphene layers with short-range order [40]. The different crystal degree of the substrates and the different forms of Pd existence indicate that the co-doped N/S plays an important role in the preparation of PdO_x-rich Pd/NS-rGO catalyst.

The scanning electron microscope (SEM) image of Pd/NS-rGO composite is shown in supporting Figure S1. It can be seen that the particles of Pd are randomly distributed over the whole area of NS dual-doped graphene and almost no agglomeration of Pt particles can be seen. The transmission electron microscope (TEM) image in Figure 2A shows that the NS co-doped graphene exhibits an extremely thin silk veil waves-like morphology and almost none significant stacking of graphene is observed. This reveal that graphite is effectively exfoliated by the modified Hummer's method. Besides, the translucent graphene nanosheets display some defects and partially crinkled nature, which may originate from the defective structure formed during the fabrication of GO and the heteroatom doping processes [41]. These defects can facilitate the chemisorption of reactants and well disperse the reduced metal particles. It can be seen that the reduced particles are uniformly dispersed with sphere-like shape and some of them coexist like nanocluster structures on the NS-rGO nano-framework support. The high-resolution TEM image in Figure 2B shows that there are two types of lattice fringes with 0.225 nm and 0.264 nm with respect to

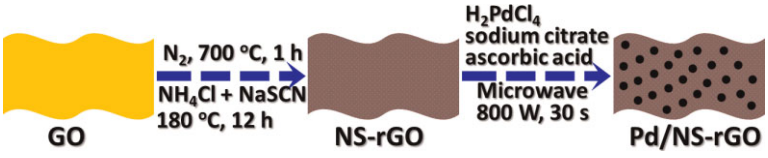

Scheme 1 Schematics of the synthetic procedures for the Pd/NS-rGO catalyst.

ORIGINAL RESEARCH PAPER

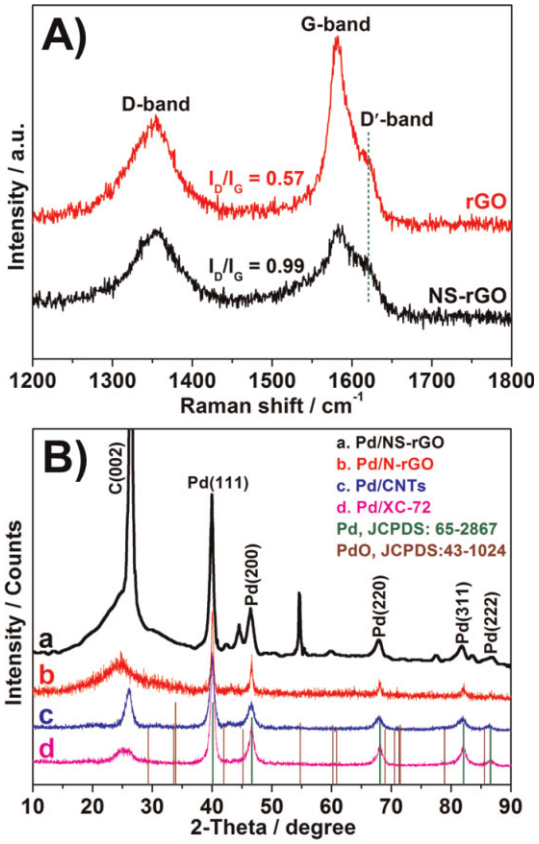

Fig. 1 (A) Raman spectra of rGO and NS-rGO. (B) XRD patterns of Pd/NS-rGO, Pd/N-rGO, Pd/CNTs and Pd/XC-72.

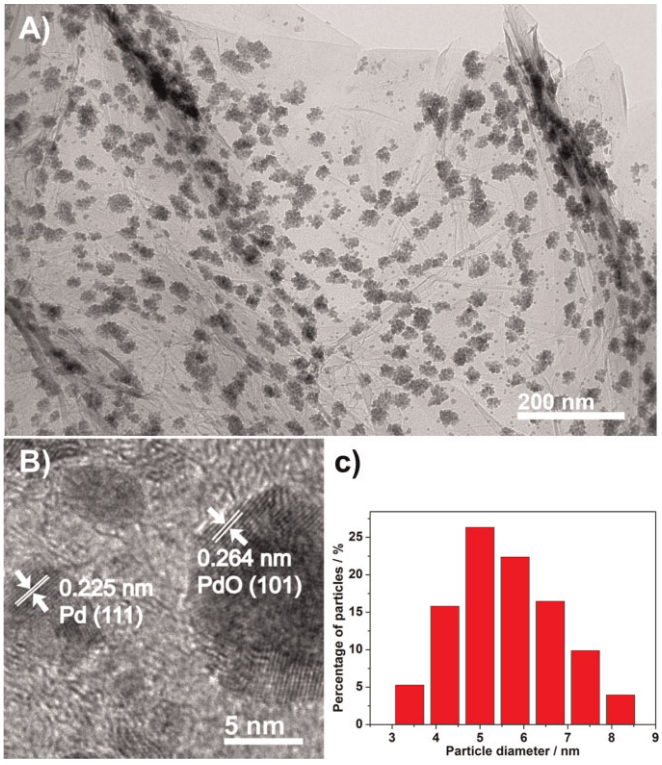

Fig. 2 (A) TEM image, (B) high-resolution TEM image and (C) particle size distribution of Pd/NS-rGO composite.

Pd (111) and PdO (101) presented on the catalyst's surface. As shown in Figure 2C, the mean size of the metal nanoparticles on NS-rGO support is obtained by measuring 200 randomly chosen particles from the magnified TEM image. For the PdO_x-rich Pd catalyst, the mean particle size has a broad distribution (3~9 nm) with an average diameter of approximately 5.4 nm. Inductively coupled plasma (ICP) was used to measure the metal loadings of various catalysts. The result shows that the loading content of Pd on NS-rGO is 19.2 wt.%, which is similar with other three compared catalysts (see Supporting Table S1). For better understanding the effect of morphologies on catalytic performance, the TEM images of other compared catalysts are further charactered as shown in Supporting Figure S2–S4. For the Pd/N-rGO catalyst, the particles distribute in two different ranges, and the average particles sizes are ~4.7 nm and ~16.8 nm, respectively. However, for the metal particles on CNTs and XC-72 carbon black, a large number of aggregated particles could be observed on their surface, and these aggregated particles maybe greatly affect their electrocatalytic performance improvement.

X-ray photoelectron spectrum (XPS) is performed to gain insight into the chemical state and surface composition of Pd, N and S in the Pd/NS-rGO sample. As shown in Supporting Figure S5, the full XPS spectrum includes C *1s*, O *1s*, N *1s*, S *2p* and Pd *3d* peaks, which indicate that the elements of N and S are successfully incorporated into graphene networks. A sharp high peak observed at ~284.4 eV certifies the existence of carbon atoms, and most of which are sp^2 hybrid carbons arranged in a conjugated honeycomb lattice of graphene. The elemental contents of N and S in Pd/NS-rGO are calculated for 2.98% and 1.82%, respectively. As shown in Figure 3A, the high-resolution spectrum of N *1s* in NS-rGO could be fitted by two peaks as for pyridine-like N (398.7 eV) and pyrrole-like N (400.8 eV) species [42]. Pyridinic N bonds with two sp^2 carbon atoms at the defects or edges of graphene can provide the π-system with one *p* electron, while pyrrolic N bonds with three sp^2 C atoms can contribute two *p* electron to the π-system, changing the valence band structure of graphene [43]. The high-resolution of S *2p* peak could be fitted with three different sulfur moieties (Figure 3B). It can be seen that the two peaks of binding energies at 162.1 eV and 167.6 eV can be assigned to the reduced (–SH) and oxidized ($–SO_n–$) sulfur moieties, respectively [44]. Additionally, another two small peaks at 163.7 eV and 165.1 eV could be clearly detected, which are in agreement with the ever reported S $2p_{3/2}$ and S $2p_{1/2}$ positions of thiophene-S owing to their spin-orbit coupling [41]. It is generally considered that co-doped two-types N and sulfur are responsible for the interaction with metal catalysts and prevent them from aggregation together [31].

The high-resolution Pd *3d* photoelectron peaks of Pd/NS-rGO catalyst are presented in Figure 3C, the binding energies for Pd $3d_{5/2}$ and Pd $3d_{3/2}$ could be resolved into three doublets. The doublet peaks with binding energies of 335.6 eV (Pd $3d_{5/2}$) and 340.9 eV (Pd $3d_{3/2}$) are attributed to

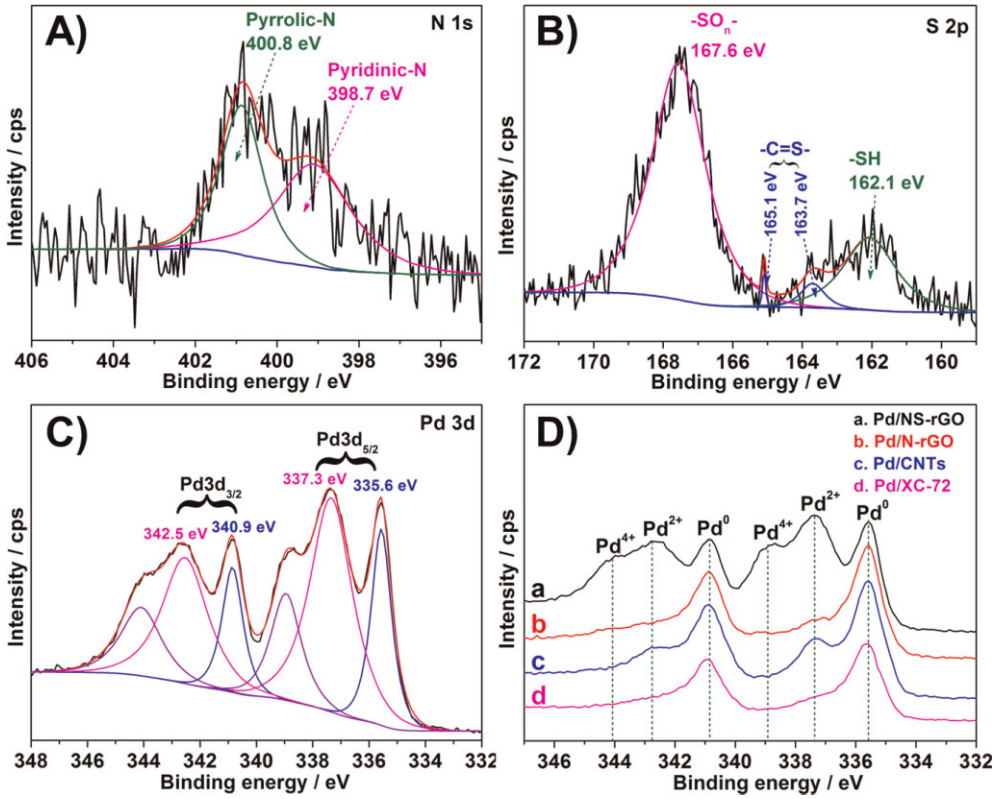

Fig. 3 High-resolution XPS spectra of (A) N *1s*, (B) S *1s* and (C) Pd *3d* of Pd/NS-rGO. (D) Comparison of the sub-spectra of Pd *3d* orbital from different catalysts.

metallic Pd [45]. The other doublet peaks with binding energies at 337.3 (Pd $3d_{5/2}$) and 342.5 eV (Pd $3d_{3/2}$) can be assigned to Pd^{2+} in PdO [46], and the binding energies at 338.9 eV (Pd $3d_{5/2}$) and 344.1 eV (Pd $3d_{3/2}$) are corresponding to PdO_2 species [47]. The spectrum of Pd *3d* indicates that the oxide of Pd (including PdO and PdO_2) is predominant in the Pd/NS-rGO composite with a relative abundance accounting for 75.7% of the total metal Pd loading, which is ~3.1-fold higher than the Pd in the form of metal Pd. Interestingly, as shown in Figure 3D, the compared four catalysts exhibit similar binding energies for Pd^0 and Pd^{2+}. It is a different phenomenon that only the as-synthesized Pd/NS-rGO sample shows the form of PdO_2 at higher binding energies. The strongest peak intensities for PdO and PdO_2 in Pd/NS-rGO catalyst illustrate that the co-doped N/S in the composite has a strong interaction force with the precursor of Pd under the same reduction conditions.

Cyclic voltammograms (CV) are executed to evaluate the electrochemical activity of Pd/NS-rGO, Pd/N-rGO, Pd/CNTs and Pd/XC-72 catalysts in N_2-saturated 0.5M NaOH solution. As shown in Figure 4A, CV curves of the different catalysts are investigated in the range of –0.8 V to 0.4 V at a scan rate of 50 mV s^{-1}. It can be seen that all catalysts have similar curve profiles and exhibit a very distinct reduction peaks at ~ –0.38 V. The reduction peaks could be ascribed to the transformation of PdO to metal Pd^0 [48], and the required coulomb charges could be used to estimate the electrochemically active surface area (EAS) of the catalysts. Generally, the coulomb charges are assumed to be the electrochemical reduction of a closed-packed monolayer of PdO on the catalyst's surface ($PdO + 2H^+ + 2e^- \leftrightarrow Pd + H_2O$) [49]. The EAS is estimated using the equation $EAS = Q/SL$ [50], where Q is the charge of electrochemical reduction of PdO in microcoulomb (μC), S (405 μC cm^{-2}) represents the proportionality constant which stands for the charge required to reduce monolayer of PdO, and L is the total amount of Pd (g) on the electrode. The calculated EAS results are listed in Table 1, and it is obviously revealed that the EAS value of Pd/NS-rGO is much larger than the ones of the other compared catalysts. The improved EAS value can be ascribed to the appearance of well-dispersed PdO_x-rich Pd on NS-rGO support and could expose much more active sites than others for interface reactions [51].

The high EAS value is generally supported by high electrocatalytic activity. Figure 4B shows the CV curves of Pd/NS-rGO together with Pd/XC-72, Pd/N-rGO and Pd/NCTs catalysts in 0.5M NaOH + 1.0M C_2H_5OH solution with a scan rate of 50 mV s^{-1}. It can be observed from CV curves that all onset potentials of the ethanol electro-oxidation begin at ~ –0.70 V, and the peak potentials of ethanol oxidation are in the range of –0.17 to –0.22 V for positive-going potential scan. In the forward-going scan, the oxidation peak is corresponding to the oxidation of freshly chemisorbed species coming from ethanol adsorption [52]. The reverse scan peak is primarily associated with removal of carbonaceous

ORIGINAL RESEARCH PAPER

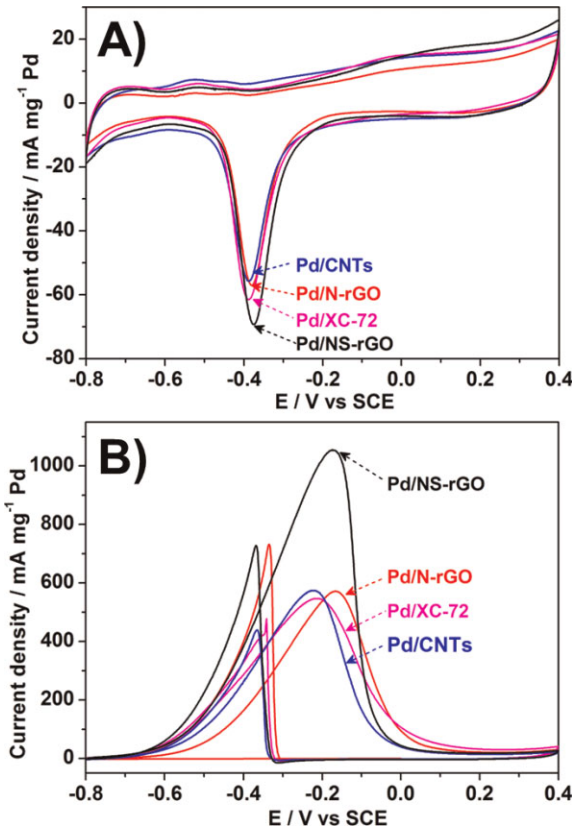

Fig. 4 Cyclic voltammograms of Pd/NS-rGO, Pd/N-rGO, Pd/CNTs and Pd/XC-72 in (A) 0.5M NaOH and (B) 0.5M NaOH + 1.0M C_2H_5OH with a scan rate of 50 mV s^{-1}.

species not completely oxidized in the forward-going scan than the oxidation of freshly chemisorbed species [53, 54]. Bianchini et al. using *In situ* FTIR spectroscopic techniques exhibited that the main forward-going oxidation product is sodium acetate at NaOH concentrations higher than 0.5M [55]. It can be seen that the current density of Pd/NS-rGO catalyst on the forward-going scan (j_f) is 1,054.0 mA mg^{-1} Pd, which is 1.84-fold higher than for Pd particles on N-rGO and CNTs catalysts and 1.93-fold higher than for the Pd/XC-72 catalyst, as shown in Table 1.

Generally, the ratio of current densities in the forward-going scan (j_f) compared to the backward-going scan (j_b) is associated with the accumulation and removal of intermediate species coming from incompletely oxidized ethanol. The ratio of j_f/j_b for Pd/NS-rGO is 1.45, which is apparently higher than that of the other three catalysts (see Table 1).

Table 1 Electrocatalytic activity of different catalysts.

Catalyst	EAS / m^2 g^{-1}	j_f / mA mg^{-1} Pd	j_b / mA mg^{-1} Pd	j_f/j_b
Pd/NS-rGO	35.7	1054.0	728.0	1.45
Pd/N-rGO	23.6	571.4	732.8	0.78
Pd/CNTs	22.5	574.0	438.0	1.31
Pd/XC-72	30.8	546.0	478.0	1.14

The excellently electrocatalytic performance and anti-poisoning intermediate species of Pd/NS-rGO catalyst could be explained by the fact that the co-doped N/S in the graphene substrate could provide enough homogeneous active sites and strong interaction force with the precursor of Pd. After the microwave-assisted ascorbic acid reduction treatment, the well-dispersed PdO_x-rich Pd particles on NS-rGO with small size are formed. It is generally considered that small sized and well dispersed particles could apparently increase the utilization of particles, and thus enlarge the EAS value and enhance the electrocatalytic performance to some extent. In addition, the concomitantly generated large proportion of PdO_x in the hybrid electrocatalysts could promote the electrocatalytic activity and anti-poisoning properties from another aspect, and it could be expressed as follows:

(i) The rich PdO_x composition in Pd/NS-rGO could better adsorb hydroxyl than metal Pd^0 [56], and the metal Pd could adsorb the dissociative ethanol molecules and then further oxidize to the resultant ethoxi, such as $(CH_3CO)_{ads}$ on the surface of metal Pd^0 when the potential run higher than onset potential (–0.7 V), see Eqs. (2)–(4):

$$PdO_x + OH^- \leftrightarrow (PdO_x)\text{–}OH_{ads} + e^- \quad (1)$$

$$Pd + OH^- \leftrightarrow Pd\text{–}OH_{ads} + e^- \quad (2)$$

$$Pd + CH_3CH_2OH \leftrightarrow Pd\text{–}(CH_3CH_2OH)_{ads} \quad (3)$$

$$Pd\text{–}(CH_3CH_2OH)_{ads} + 3OH^- \rightarrow Pd\text{–}(CH_3CO)_{ads} + 3H_2O + 3e^- \quad (4)$$

(ii) The $(CH_3CO)_{ads}$ are strongly adsorbed onto the active sites of the Pd^0 surface and it can be stripped off from the Pd^0 surface by the adsorbed hydroxyl species [57]. As a result, the ethanol could be continuously oxidized with increase of the potential, i.e., Eqs. (5)–(6):

$$Pd\text{–}(CH_3CO)_{ads} + (PdO_x)\text{–}OH_{ads} \leftrightarrow Pd + PdO_x + CH_3COOH \quad (5)$$

$$Pd\text{–}(CH_3CO)_{ads} + Pd\text{–}OH_{ads} \leftrightarrow Pd + CH_3COOH \quad (6)$$

(iii) After the potential runs to the peak current density, it will start to decline with a further increase of the potential. The decreased in current density is considered relevant to the formation of Pd(II) oxide layer on the surface of the electrode at higher potentials [58]. The formed oxide layer could block the adsorption of fresh ethanol molecules onto Pd^0 surface and thus lead to a decrease in the electrocatalytic activity.

Stability is another important criterion to evaluate a developed catalyst. Thus, long-term stability was conducted in a solution of 0.5M NaOH + 1.0M C_2H_5OH for 7,200 s at a fixed potential of –0.2 V. As shown in Figure 5, it could be observed

that all catalysts initially display a sharp current density decay, and then turn into a pseudo-steady state. As shown the insert chart in Figure 5, it could be observed that the current density of Pd/NS-rGO catalyst is 109.5 mA mg^{-1} Pd after running 7,200 s, which is 1.84, 3.40 and 1.53-fold higher than Pd/N-rGO, Pd/CNTs and Pd/XC-72, respectively. The admirable stability of Pd/NS-rGO catalyst could be regarded relevant with well-dispersed Pd particles, the stronger binding force between Pd and co-doped N and S to inhibit agglomeration of particles, and rich-PdO_x provided lots of adsorption hydroxyl to remove intermediate species.

4 Conclusions

In this work, we have demonstrated a facile process to synthesize NS co-doped graphene supported PdO_x-rich Pd electrocatalysts *via* microwave-assisted ascorbic acid reduction method. The NS co-doped graphene provide uniformly active sites to deposited PdO_x-rich Pd particles. The stronger binding force between PdO_x-rich Pd particles and the support successfully suppressed the particles exfoliation and agglomeration after long-time stability testing. In addition, the Pd/NS-rGO catalyst also revealed a larger electrochemically active surface area, higher forward current density and tolerance to intermediate species poisoning. The well-dispersed PdO_x-rich Pd particles on NS co-doped graphene in this study possess excellent electrocatalytic properties and stability for ethanol electrooxidation in alkaline media and may be of great potential regarding ethanol sensor and direct ethanol fuel cells.

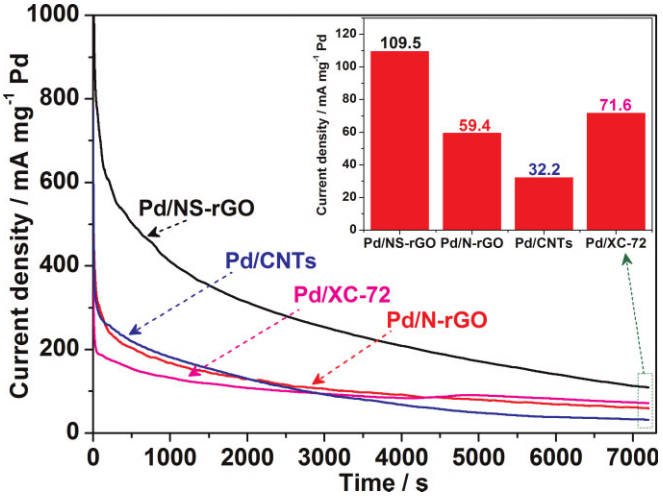

Fig. 5 Long-term stability curves of the Pd/NS-rGO, Pd/N-rGO, Pd/CNTs and Pd/XC-72 catalysts at –0.2 V for 7,200 s in 0.5M NaOH + 1.0M C_2H_5OH solution. The inset image shows the last values of chronoamperometric curves for these four catalysts.

Acknowledgements

This work has been supported by the National Natural Science Foundation of China (21163002, 21165004, 21363003), Natural Science Foundation of Guangxi Province (2014GXNSFFA118003, 2014GXNSFGA118008), BAGUI scholar program (2014A001), Project of Talents Highland of Guangxi Province and Guangxi Key Laboratory of Low Carbon Energy Materials.

References

[1] X. Huang, Z. Zhao, L. Cao, Y. Chen, E. Zhu, Z. Lin, M. Li, A. Yan, A. Zettl, Y. M. Wang, X. Duan, T. Mueller, Y. Huang, *Science* **2015**, *348*, 1230.
[2] D. Wang, H. L. Xin, R. Hovden, H. Wang, Y. Yu, D. A. Muller, F. J. DiSalvo, H. D. Abruña, *Nat. Mater.* **2013**, *12*, 81.
[3] Z. Yin, B. Chen, M. Bosman, X. Cao, J. Chen, B. Zheng, H. Zhang, *Small* **2014**, *10*, 3537.
[4] G. Wang, L. Zhang, J. Zhang, *Chem. Soc. Rev.* **2012**, *41*, 797.
[5] C. W. Xu, H. Wang, P. K. Shen, S. P. Jiang, *Adv. Mater.* **2007**, *19*, 4256.
[6] E. Antolini, *Energy Environ. Sci.* **2009**, *2*, 915.
[7] Y. Feng, L. Bu, S. Guo, J. Guo, X. Huang, *Small* **2016**, *12*, 4464.
[8] K. Tran, T. Q. Nguyen, A. M. Bartrom, A. Sadiki, J. L. Haan, *Fuel Cells* **2014**, *14*, 834.
[9] H. Takahashi, M. Sagihara, M. Taguchi, *Int. J. Hydrog. Energy* **2014**, *39*, 18424.
[10] Z. Chen, D. Higgins, A. Yu, L. Zhang, J. Zhang, *Energy Environ. Sci.* **2011**, *4*, 3167.
[11] V. Rao, Hariyanto, C. Cremers, U. Stimming, *Fuel Cells* **2007**, *7*, 417.
[12] S. Beyhan, J.-M. Léger, F. Kadırgan, *Appl. Catal. B-Environ.* **2013**, *130–131*, 305.
[13] W. Du, N. A. Deskins, D. Su, X. Teng, *ACS Catal.* **2012**, *2*, 1226.
[14] Y.-h. Li, Q.-z. Xu, Q.-Y. Li, H. Wang, Y. Huang, C.-w. Xu, *Electrochim. Acta* **2014**, *147*, 151.
[15] B. Liu, Z. W. Chia, Z. Y. Lee, C. H. Cheng, J. Y. Lee, Z. L. Liu, *Fuel Cells* **2012**, *12*, 670.
[16] J. J. Li, J. S. Wang, X. Guo, J. H. Zhao, C. Y. Song, L. C. Wang, *Fuel Cells* **2012**, *12*, 898.
[17] A. Zubiaur, M. Chatenet, F. Maillard, S. D. Lambert, J. P. Pirard, N. Job, *Fuel Cells* **2014**, *14*, 343.
[18] Z. Zhang, L. Xin, K. Sun, W. Li, *Int. J. Hydrog. Energy* **2011**, *36*, 12686.
[19] Y. Zhang, H. Shu, G. Chang, K. Ji, M. Oyama, X. Liu, Y. He, *Electrochim. Acta* **2013**, *109*, 570.
[20] G.-J. Chen, J.-S. Wang, F.-Z. Jin, M.-Y. Liu, C.-W. Zhao, Y.-A. Li, Y.-B. Dong, *Inorg. Chem.* **2016**, *55*, 3058.

[21] M. Sawangphruk, A. Krittayavathananon, N. Chinwipas, P. Srimuk, T. Vatanatham, S. Limtrakul, J. S. Foord, *Fuel Cells* **2013**, *13*, 881.
[22] N. O. Weiss, H. Zhou, L. Liao, Y. Liu, S. Jiang, Y. Huang, X. Duan, *Adv. Mater.* **2012**, *24*, 5782.
[23] Z. Fang, Y. Wang, Z. Liu, A. Schlather, P. M. Ajayan, F. H. L. Koppens, P. Nordlander, N. J. Halas, *ACS Nano* **2012**, *6*, 10222.
[24] C.-B. Ma, X. Qi, B. Chen, S. Bao, Z. Yin, X.-J. Wu, Z. Luo, J. Wei, H.-L. Zhang, H. Zhang, *Nanoscale* **2014**, *6*, 5624.
[25] C. L. He, Y. X. Jiang, L. Rao, Q. Wang, B. W. Zhang, Y. Y. Li, S. G. Sun, *Fuel Cells* **2013**, *13*, 873.
[26] M. Wu, Q. Tang, F. Dong, Y. Wang, D. Li, Q. Guo, Y. Liu, J. Qiao, *Phys. Chem. Chem. Phys.* **2016**, *18*, 18665.
[27] X. Zhou, S. Tang, Y. Yin, S. Sun, J. Qiao, *Appl. Energy* **2016**, *175*, 459.
[28] F. Cao, M. Zhao, Y. Yu, B. Chen, Y. Huang, J. Yang, X. Cao, Q. Lu, X. Zhang, Z. Zhang, C. Tan, H. Zhang, *J. Am. Chem. Soc.* **2016**, *138*, 6924.
[29] B. P. Vinayan, R. Nagar, S. Ramaprabhu, *J. Mater. Chem. A* **2013**, *1*, 11192.
[30] J. Y. Kim, N.-J. Choi, H. J. Park, J. Kim, D.-S. Lee, H. Song, *J. Phys. Chem. C* **2014**, *118*, 25994.
[31] X. Zhang, J. Zhu, C. S. Tiwary, Z. Ma, H. Huang, J. Zhang, Z. Lu, W. Huang, Y. Wu, *ACS Appl. Mater. Interfaces* **2016**, *8*, 10858.
[32] W. Ai, Z. Luo, J. Jiang, J. Zhu, Z. Du, Z. Fan, L. Xie, H. Zhang, W. Huang, T. Yu, *Adv. Mater.* **2014**, *26*, 6186.
[33] J. Xu, G. Dong, C. Jin, M. Huang, L. Guan, *ChemSusChem* **2013**, *6*, 493.
[34] Y. Zhao, X. Yang, J. Tian, *Electrochim. Acta* **2009**, *54*, 7114.
[35] Y. Zhao, X. Yang, J. Tian, F. Wang, L. Zhan, *J. Power Sources* **2010**, *195*, 4634.
[36] P. Liu, G. Li, W.-T. Chang, M.-Y. Wu, Y.-X. Li, J. Wang, *RSC Adv.* **2015**, *5*, 72785.
[37] Y. Zhao, X. Yang, J. Tian, F. Wang, L. Zhan, *Mater. Sci. Eng. B* **2010**, *171*, 109.
[38] B. G. Abraham, K. K. Maniam, A. Kuniyil, R. Chetty, *Fuel Cells* **2016**, *16*, 656.
[39] X. Yang, J. Zheng, M. Zhen, X. Meng, F. Jiang, T. Wang, C. Shu, L. Jiang, C. Wang, *Appl. Catal., B* **2012**, *121–122*, 57.
[40] B. P. Vinayan, R. Nagar, N. Rajalakshmi, S. Ramaprabhu, *Adv. Funct. Mater.* **2012**, *22*, 3519.
[41] S. Yang, L. Zhi, K. Tang, X. Feng, J. Maier, K. Müllen, *Adv. Funct. Mater.* **2012**, *22*, 3634.
[42] W. Si, J. Zhou, S. Zhang, S. Li, W. Xing, S. Zhuo, *Electrochim. Acta* **2013**, *107*, 397.
[43] X. Du, D. Jiang, Q. Liu, J. Qian, H. Mao, K. Wang, *Talanta* **2015**, *132*, 146.
[44] Y. Su, Y. Zhang, X. Zhuang, S. Li, D. Wu, F. Zhang, X. Feng, *Carbon* **2013**, *62*, 296.
[45] T. Shobha, C. L. Aravinda, P. Bera, L. G. Devi, S. M. Mayanna, *Mater. Chem. Phys.* **2003**, *80*, 656.
[46] X. Yang, M. Zhen, G. Li, X. Liu, X. Wang, C. Shu, L. Jiang, C. Wang, *J. Mater. Chem. A* **2013**, *1*, 8105.
[47] I. G. Casella, M. Contursi, *Electrochim. Acta* **2006**, *52*, 649.
[48] K. Kakaei, M. Dorraji, *Electrochim. Acta* **2014**, *143*, 207.
[49] T. Chierchie, C. Mayer, W. J. Lorenz, *J. Electroanal. Chem. Interfacial Electrochem.* **1982**, *135*, 211.
[50] Y. Zhao, S. Nie, H. Wang, J. Tian, Z. Ning, X. Li, *J. Power Sources* **2012**, *218*, 320.
[51] S. K. Meher, G. R. Rao, *ACS Catal.* **2012**, *2*, 2795.
[52] Q. Cui, S. Chao, Z. Bai, H. Yan, K. Wang, L. Yang, *Electrochim. Acta* **2014**, *132*, 31.
[53] J. Liu, J. Ye, C. Xu, S. P. Jiang, Y. Tong, *Electrochem. Commun.* **2007**, *9*, 2334.
[54] N. Li, Y.-X. Zeng, S. Chen, C.-W. Xu, P.-K. Shen, *Int. J. Hydrog. Energy* **2014**, *39*, 16015.
[55] X. Fang, L. Wang, P. K. Shen, G. Cui, C. Bianchini, *J. Power Sources* **2010**, *195*, 1375.
[56] P. Jayaweera, S. Hettiarachchi, H. Ocken, *Colloid Surf. A-Physicochem. Eng.* **1994**, *85*, 19.
[57] Z. S. Yang, J. J. Wu, *Fuel Cells* **2012**, *12*, 420.
[58] Z. X. Liang, T. S. Zhao, J. B. Xu, L. D. Zhu, *Electrochim. Acta* **2009**, *54*, 2203.

